Volume 1 | Number 1 | Jan 2013 | Pages 1–100

Nanoscale

www.rsc.org/nanoscale

ROYAL SOCIETY OF CHEMISTRY

ROYAL SOCIETY OF CHEMISTRY

www.rsc.org/nanoscale

Journal Name

ARTICLE

Long-circulating PEGylated Manganese Ferrite Nanoparticles for MRI-based molecular imaging

Manuel Pernia Leal,[a]* Sara Rivera-Fernández,[b] Jaime M. Franco,[c] David Pozo,[c,d] Jesús M. de la Fuente[b,e,f] and María Luisa García-Martín[a]*

Magnetic Resonance based Molecular Imaging has emerged as a very promising technique for early detection and treatment monitoring of a wide variety of diseases, among them, cancer, neurodegenerative disorders, and vascular diseases. The limited sensitivity and specificity of conventional MRI are being overcome by the development of a new generation of contrast agents, using nanotechnology approaches, with improved magnetic and biological properties. In particular, for molecular imaging, high specificity, high sensitivity, and long blood circulation times are required. Furthermore, lack of toxicity and immunogenicity, together with low-cost scalable production are also necessary to get them into the clinics. In this work, we describe a facile, robust and cost-effective ligand-exchange method to synthesize dual T_1 and T_2 MRI contrast agents with long circulation times. These contrast agents are based on manganese ferrite nanoparticles (MNPs) between 6 and 14 nm size, covered by a 3 kDa polyethylene glycol (PEG) shell that leads to a great stability in aqueous media with high crystallinity and magnetization values, thus keeping the magnetic properties of the uncovered MNPs. Moreover, the PEGylated MNPs have shown different relaxivities depending on their size and magnetic field. Thus, the 6 nm PEGylated MNPs are characterized by a low r_2/r_1 ratio of 4.9 at 1.5 T, hence resulting in a good dual T_1 and T_2 contrast agent at low fields, whereas the 14 nm MNPs behave as excellent T_2 contrast agent at high fields ($r_2 = 335.6$ mM^{-1}s^{-1}). The polymer core shell of the PEGylated MNPs minimizes their cytotoxicity, and permits long blood circulation times. This combination of cellular compatibility, excellent T_2 and r_2/r_1 values at low fields, together with long circulation times, make these nanomaterials very promising contrast agents for molecular imaging.

Introduction

Magnetic nanoparticles have been investigated in the last decade for multiple purposes in nanomedicine such as drug delivery nanocarriers, hyperthermia and magnetic resonance imaging contrast agents.[1-7] In the field of MRI contrast agents, many efforts have been undertaken to develop more powerful and sensitive materials that on the one hand could improve the current contrast agents in terms of relaxation times, both longitudinal or T_1, and transverse or T_2, and on the other hand, could increase the circulation time and reduce cytotoxicity. MRI contrast agents are sorted in two types: T_1 contrast agents, which are commonly called positive contrast agents due to the signal enhancement they produce on T_1-weighted images; and T_2 or negative contrast agents, which produce darkening on T_2-weighted images. The ability of given contrast agent to decrease the T_1 or T_2 relaxation times of the surrounding water protons is called relaxivity, r_1 or r_2 (expressed in mM^{-1}s^{-1}), and the ratio r_2/r_1 indicates the capacity of the material to be used as

T_1 or T_2 contrast agent.[8] Lower values of r_2/r_1 (between 1-3) lead to T_1 type, higher values (> 10) to T_2 type, and the intermediate values, between 3-10, can be considered as dual T_1 and T_2 contrast agents.

Gadolinium (Gd) chelates are the most commonly used MRI contrast agents in the clinical practice. They produce T_1 shortening of the water protons through chemical exchange of the coordinated water with the bulk water, which translates into signal enhancement on T_1-weigthed images (positive contrast). These contrast agents are rapidly excreted through renal filtration and are normally used to visualize areas with leaky vessels (inflammation, tumors, etc.), where they are retained due to the enhanced permeability and retention (EPR) effect or passive targeting. For molecular imaging, which is typically based on active targeting, longer circulation times and higher sensitivity are required. Gd nanoparticles arose as a promising alternative to Gd chelates because they combine both very high relaxivity, due to the concentration of Gd ions per nanoparticle, and long circulation times. However, it has been shown that Gd

ions, leached from either complexes or nanoparticles could become highly toxic *in vivo*, thus leading to important renal problems such as nephrogenic systemic fibrosis.[9] On the contrary, superparamagnetic iron oxide nanoparticles (SPIONs) show very low toxicity. Indeed, SPIONs have been approved by the FDA and have been applied successfully in the clinical practice as bowel contrast agent (i.e., Lumiren® and Gastromark®) and also for liver/spleen imaging (i.e., Endorem® and Feridex IV®). Another advantage of SPIONs is that they can be easily synthesized with size control and low cost production via thermal decomposition methods.[10] In terms of relaxivity, they show very high r_2/r_1 values, being postulated good T_2-type contrast agents for molecular imaging.[11] However, one of the main concerns regarding T_2 contrast is that the T_2-weighted MRI sequences used to visualize the signal voids they produce are prone to susceptibility artifacts caused by air, hemorrhage or metal implants, which can lead to misinterpretations, and consequently positive contrast is usually preferred.

It was recently reported that decreasing the size of the iron oxide nanoparticles below 4 nm enhances their efficiency as T_1 contrast agents and hence it could be used as a strategy to obtain dual contrast agents. Unfortunately the increase in r_1 was accompanied by a significant decrease of r_2, leading to low r_2/r_1 values, and limiting the use of these nanoparticles as T_1 contrast agents.[12] Manganese doped-iron oxide nanoparticles are good candidates to overcome this limitation. The incorporation of a paramagnetic ion in the spinel ferrite structure induces an increase in the mass magnetization of the material leading to an improvement of the magnetic properties of the materials.[4, 13-17] The use of manganese for biomedical application, however, brings another concern into the picture, the high toxicity of Mn^{2+} ions.[18] It becomes then crucial to avoid metal leaching from the nanoconjugates. Many different coating strategies have been developed to protect the inorganic core of the magnetic nanoparticles from the surrounding media, and to increase their stability in biological environments.[19] The coating strategies can be sorted in two main categories, the micellar encapsulation[20] and the ligand exchange. Micellar encapsulation is the most universal and extended method, based on the addition of a second layer of an amphiphilic polymer that interacts in a non-covalent manner with the outer hydrophobic layer of the nanoparticle. This interaction is not stable enough and further functionalizations are required to enforce the stability of the organic shell around the inorganic core. The other coating strategy, ligand exchange, requires the use of a ligand molecule much more reactive and with stronger binding than the surfactant attached to the nanoparticle during the nanoparticle synthesis. Thus, a standard ligand molecule would present an anchor group in one side that binds to the nanoparticle surface and a reactive group on the other side. The stability in aqueous media of the ligand-exchanged magnetic nanoparticles depends somehow on the binding interaction between the anchor group of the ligand and the surface of the magnetic nanoparticles, and also on the hydrophilic balance of the functionalized nanoparticles.[21, 22] The polyethylene glycol (PEG) chain is an ideal hydrophilic spacer for the ligand exchange because it not only modulates the hydrophilic balance of the magnetic nanoparticles, but also supports resistance to protein adsorption and helps the nanoparticles to improve their circulation life time and to decrease the reticuloendothelial clearance rate.[23, 24]

We report herein a facile method to functionalize manganese ferrite nanoparticles (MNPs) by a simple ligand exchange. The ligand molecule presents an anchor group (gallol derived) that binds strongly to the MNP surface[25] and a tunable and biocompatible hydrophilic PEG part that allows the stabilization of the MNPs in aqueous media. Also, the ligand exchange takes place by a gentle shaking in few seconds without perturbing the magnetic characteristics of the manganese ferrite nanoparticles. Furthermore, we demonstrate the possibility to tune the relaxivities r_1 and r_2 of PEGylated MNPs based on their size and their use as MRI contrast agents with long circulation times and potential tumour targeting.

Results and Discussion

Synthesis of water soluble Manganese Ferrite Nanoparticles

Monodisperse manganese ferrite nanoparticles (MNPs) with different diameter sizes were synthesized by following the seed-mediated growth protocol previously described by Sun and coworkers.[26] The 6 nm MNP seeds were synthesized and by a successive growth, 7.5, 9, 12 and 14 nm MNPs, were synthesized. These MNPs were capped with oleic acid to stabilize them in organic solvents such as toluene or hexane, but a further approach is required to transfer them to aqueous media. The easy and novel proposed approach to render hydrophilic manganese ferrite nanoparticles is based on the ligand exchange method developed by us on super-paramagnetic iron oxide nanoparticles (SPIONs). The success of this approach, reported elsewhere,[22] lied on several factors: i) high yield and stability of SPIONs in aqueous media and ii) low-cost and facile synthesis of the PEG-Gallol derived ligand with the possibility to modify further the end group of the PEG chain (for instance -OH or –NH_2). Therefore, we synthesized the Gallol-PEG-OH ligand following the reported procedure (see Experimental Section) with a modification in the length of the PEG chain to 3000 Da of molecular weight. We have chosen a 3000 Da PEG spacer because it is within the optimal molecular weight range (1500-5000 Da) to minimize the phagocytic response of macrophages thus extending the nanoparticles circulation time.[27] The anchor of the ligand is the gallol group, which probably reacts through strong electrostatic interactions between the MNP surface and the hydroxyl groups of the gallol derived in the same way as iron oxide nanoparticles. The ligand exchange procedure (see details in Experimental Section) takes place by a gentle shaking in the presence of a nucleophilic base as triethylamine (Fig. 1A). Indeed, the replacement occurs smoothly and instantaneously, thus leading to water soluble manganese ferrite nanoparticles.
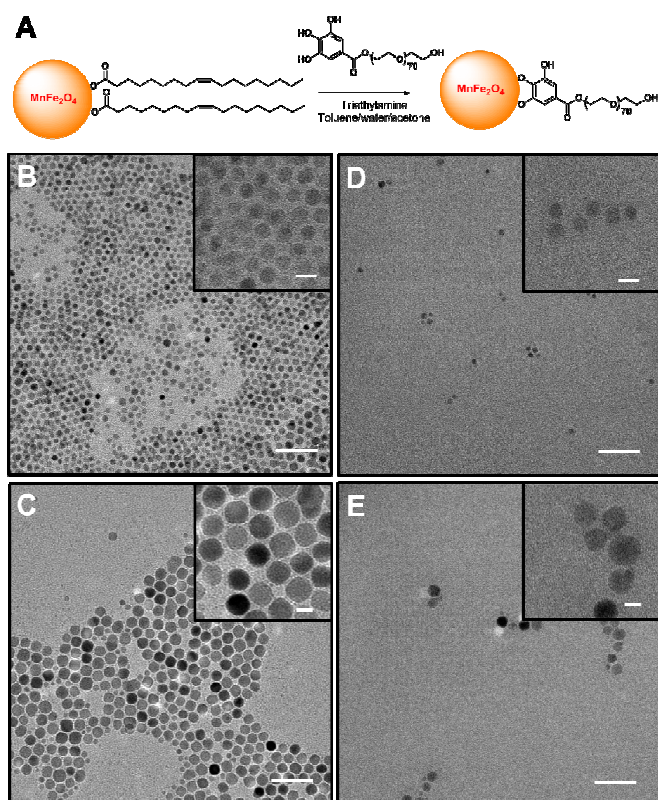
Fig. 1. Characterization of manganese ferrite nanoparticles (MNPs) by Transmission Electron Microscopy (TEM). A) Scheme of ligand exchange on manganese ferrite nanoparticles (MNPs). Representative TEM images at low magnification of as-prepared MNPs with diameters of 6 nm (B) and 14 nm (C), and water soluble ligand exchanged MNPs with diameters of 6 nm (D) and 14 nm (E). Insets B-E correspond to high magnification TEM images. Scale bars correspond to 50 nm for low magnification TEM images and 10 nm for the insets.

One of the main problems during the transfer of the NPs to water is the aggregation with the consequent precipitation of the particles and the modification and/or loss of their magnetic properties. This aggregation could be possibly related to several physicochemical factors such as weak ligand-NP interactions, poor hydrophilic/hydrophobic balance, and surface charge density among others.[28] Also, it is important to take into account the physiological factors that could affect the magnetic properties and stability of the MNPs *in vivo* (discussed in detailed in the *in vivo* MRI studies section). In our procedure, the two first problems are solved with the use of a gallol derived and a 3000 Da PEG spacer; the third one, the surface charge density over the nanoparticle, is solved by minimizing the charges of the ligand, the more neutral it is, the more stable our nanoparticles will be. Therefore, the end group of the ligand in our case is a hydroxyl group. Moreover, that functionality will allow us to attach vectors such as biomolecules or drugs for targeting and treatment of different diseases in future investigations.

Characterization of water soluble MNPs

As mentioned above, the properties of the nanoparticles could potentially be affected with the functionalization. To demonstrate that our ligand exchange method on manganese ferrite nanoparticles does not affect the magnetic and physicochemical properties of the *as-prepared* nanoparticles, we performed an exhaustive characterization of the MNPs in water solution. Firstly, the mean diameter sizes of the MNPs were determined by TEM and dynamic light scattering (DLS). TEM characterization could not confirm the presence of the Gallol-PEG-OH on the MNPs, but it was observed that the Gallol-PEG-MNPs were well dispersed and separated on the TEM grid with respect to the *as-prepared* MNPs (Fig. 1B-D, and Fig. S1 and S2). On the contrary, by DLS we could observe a notable increase (between 14 and 19 nm) in the hydrodynamic diameter of the manganese nanoparticles, indicating a change in the coating of the MNPs (Fig. 2A). Moreover, negative and minimum (Z)-potential values were measured under physiological pH and osmolality conditions for the water soluble MNPs (Fig. 2A), in accordance with the premises commented above for long-time circulation nanoparticles *in vivo*. Then, the presence of the ligand Gallol-PEG-OH attached to the MNPs was confirmed by FTIR spectroscopy, the FTIR spectrum exhibited the corresponding signals to the PEG in comparison with the starting manganese ferrite nanoparticles, which exhibited the oleic acid (surfactant) signals (Fig. 2B, and Fig. S3).
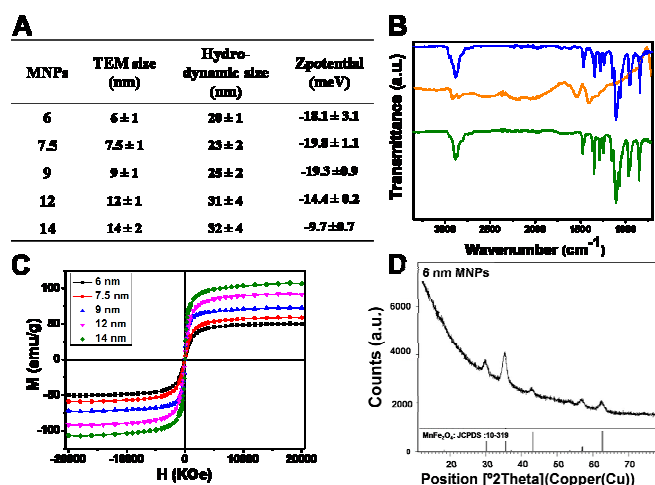

Fig. 2. Physicochemical characterization of manganese ferrite nanoparticles. A) Diameters determined by TEM and DLS measurements, and Z-potential values of the MNP-GA-PEG-OH under physiological conditions. B) FTIR spectra of as-prepared MNPs (orange curve), ligand GA-PEG-OH (blue curve) and 6 nm MNP-GA-PEG-OH (green curve). C) Field-dependent magnetization curves (M-H) measured at 298 K for MNP-GA-PEG-OH with diameters of 6 nm (black), 7.5 nm (red), 9 nm (blue), 12 nm (pink) and 14 nm (green). D) Powder X-ray diffraction pattern of 6 nm MNP-GA-PEG-OH and reference XRD pattern of $MnFe_2O_4$.

To demonstrate that the signals corresponded to the ligand attached to the manganese ferrite nanoparticles and they were not due to the ligand in solution, two different purification methods were applied: i) dialysis through a membrane (MWCO: 25 kDa) during 3 days exchanging milli-Q water at 3 and 8 hours with fresh milli-Q water, and ii) further purification into a centrifugal PALL filter (MWCO: 100 kDa) at 450 rcf, being this step repeated until a clear solution was obtained (Fig. S4 and Fig. S5). It was observed that during the first purification by dialysis, the MNPs did not collapse, thus indicating the high stability of the functionalized MNPs in water. The percentage of the organic shell around the MNPs was evaluated by thermo-gravimetric analysis (TGA), giving a range of 42-53% of organic material (Fig. S6). Based on the TGA results and the TEM average diameters, the dispersant packing density revealed a proportional increase from 1.1 to 2.8 molecules per nm^2 for the 6 and 14 nm PEGylated MNPS respectively. This corresponds to higher dispersant packing density values for larger nanoparticles due to lower steric hindrance among the ligands (Table S1). The magnetic properties of the MNPs (6, 7.5, 9, 12 and 14 nm) were investigated by Vibrating Sample Magnetometer (VSM) at room temperature. The values of mass magnetization (Ms) of the water soluble MNPs were in good agreement with the findings obtained by Cheon and coworkers for manganese-doped iron oxide nanoparticles,[4] in which the bigger the magnetic nanoparticles, the higher the Ms values, thus showing Ms values of 50, 60, 72, 92 and 106 emu/g (Mn+Fe) for 6, 7.5, 9, 12 and 14 nm size water soluble manganese ferrite nanoparticles, respectively (Fig. 2C). In addition, X-ray diffraction (XRD) analysis of the MNPs revealed that the mild conditions of ligand exchange did not affect the structure of the nanoparticles observing the characteristic peaks for the ferromagnetic spinel phase (Fig. 2D, and Fig. S7).

To evaluate the feasibility of the MNP-GA-PEG-OH as potential T_1 and T_2 MRI contrast agents, the relaxivities were measured on a 1.5 T relaxometer, and a 9.4 T pre-clinical MRI scanner. In the case of transverse relaxivity, r_2 a similar trend was observed in both magnetic resonance spectrometers (1.5 and 9.4 T), bigger size MNPs (such as 14 nm) exhibited higher relaxivity values (301 and 336 $mM^{-1}s^{-1}$ respectively) in agreement with the mass magnetization values trend (Fig. 3A). This means that the Ms value of the manganese ferrite nanoparticle directly correlates with NP size, as commented above, due to well-known spin canting effects that affect the smaller magnetic nanoparticles dramatically, and in the same degree their r_2.[29] On the contrary, r_1 did not show the same trend, being significant at low magnetic field, but negligible at high field (Fig. 3B). This might be due to the fact that r_1 is dominated mainly by interactions between bulk water protons and electron spins of the nanoparticles, and the diffusion time of water close to the inner sphere of the MNP.[30] Therefore, the r_1 values for the MNPs-GA-PEG-OH were found similar independently of their sizes, between 7 and 18 $mM^{-1}s^{-1}$ at 1.5 T, but with a resulting $r_2/r_1 < 5$ for the smaller MNPs (6 and 7.5

nm). This r_2/r_1 values fall within the intermediate range that characterizes dual T_1 and T_2 contrast agents. In contrast, at 9.4 T the r_2/r_1 ratios increased dramatically, above 78, for 6 and 7.5 nm MNPs because at very high magnetic fields r_1 decreases to values proximate to zero, whereas r_2 increases, which limits the use of these MNPs-GA-PEG-OH as T_2 contrast agents at the high fields typically used in preclinical studies (Fig. 3C). Therefore, for the in vivo studies in animal models we used T_2-weighted MRI sequences, as discussed in detail below. However, it is noteworthy to mention that at clinical magnetic fields they could be used as dual contrast agents, i.e., both T_1 and T_2, which is the ultimate goal of the PEGylated nanoparticles developed in the current work.
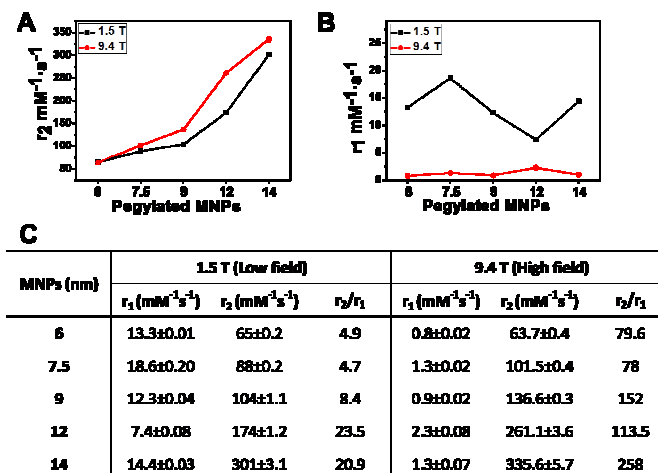

Fig. 3. Relaxivity measurements of MNP-GA-PEG-OH at low and high magnetic fields. A) Transverse relaxivity coefficient, r_2, values of different sizes of MNP-GA-PEG-OH at 1.5 T (black) and 9.4 T (red). B) Longitudinal relaxivity, r_1, values of different sizes of MNP-GA-PEG-OH at 1.5 T (black) and 9.4 T (red). C) Summary of relaxivities values of MNP-GA-PEG-OH at low and high magnetic field.

MNPs (nm)	1.5 T (Low field)			9.4 T (High field)		
	r_1 ($mM^{-1}s^{-1}$)	r_2 ($mM^{-1}s^{-1}$)	r_2/r_1	r_1 ($mM^{-1}s^{-1}$)	r_2 ($mM^{-1}s^{-1}$)	r_2/r_1
6	13.3±0.01	65±0.2	4.9	0.8±0.02	63.7±0.4	79.6
7.5	18.6±0.20	88±0.2	4.7	1.3±0.02	101.5±0.4	78
9	12.3±0.04	104±1.1	8.4	0.9±0.02	136.6±0.3	152
12	7.4±0.08	174±1.2	23.5	2.3±0.08	261.1±3.6	113.5
14	14.4±0.03	301±3.1	20.9	1.3±0.07	335.6±5.7	258

Cell Viability

Key factors that influence further developments of engineered nanoparticles for biological applications are first related to cellular biocompatibility. In this sense, we carried out three different experimental settings to assess cell metabolic activity, cell membrane integrity and cell cycle as readouts of cell viability (Fig. 4). We used a human prostate cancer cell line, PC-3, as a working model. The cell exposure to increasing concentrations of MNP-GA-PEG-OH from 0.1 µg/mL up to 100 µg/mL for 24 h was shown not to be detrimental, as the MTT activity was maintained around or above 80% of the non-treated cells for all the concentrations tested, irrespective of the size of the nanoparticles used (Fig. 4A). When we measured the extracellular LDH activity in PC-3 treated cells as a surrogate marker of death cell, we did not observe a substantial effect at different nanoparticle concentrations and sizes, except for the highest concentration corresponding to 100 µg/mL (Fig. 4B). The latter LDH reduction is consistent with the lower MTT values noted in PC-3 cells treated at the highest concentration of MNP-GA-PEG-OH, suggesting a mild decrease in the cell

number. This is in close agreement with the flow cytometry data performed at the highest dose of nanoparticles. As it is shown in the scatter plot, PC-3 treated cells were no necrotic and the analysis of the subG1 cell cycle revealed no features of apoptosis, with no differences compared to untreated PC-3 cells (Fig. 4C). Thus, taken together MNP-GA-PEG-OH with a ranging size from 6 to 14 nm seem to be compatible with key parameters related to cell viability.
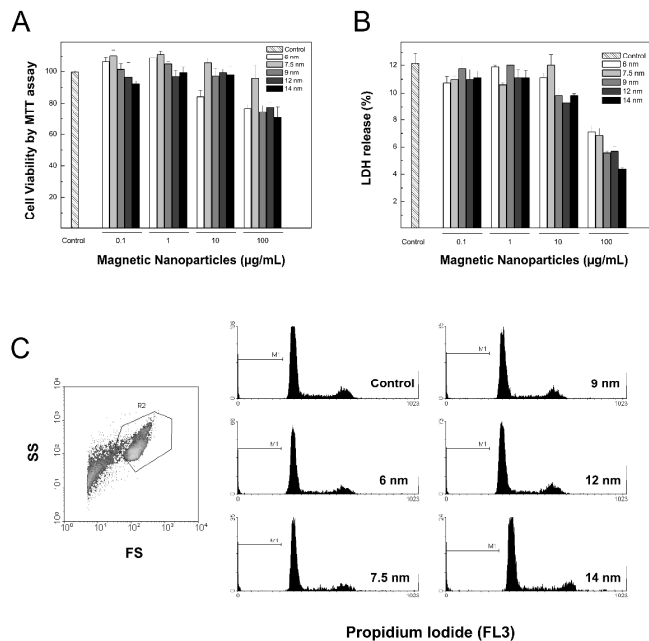

Fig. 4. Effects of MNP-GA-PEG-OH on cell biocompatibility. A) Metabolically active cells were determined by MTT assay of human PC-3 cells treated for 24 h with MNP-GA-PEG-OH at various concentrations. B) Cytotoxicity was determined by LDH assay on supernatants from human PC-3 cells treated cells for 24 h with MNP-GA-PEG-OH at various concentrations. C) Apoptosis was evaluated by flow cytometry in human PC-3 cells treated for 24 h with MNP-GA-PEG-OH at 100 ug/ml. The left panel shows the scatter plot, and the histograms show the SubG1 region (M1 bar).

In vivo MRI Studies

For *in vivo* studies, two extreme manganese nanoparticles were chosen based on their size and relaxivity values, the smallest one, 6 nm MNP-GA-PEG-OH, which presents a hydrodynamic diameter in physiological medium of 20 nm and a r_2 of 64 mM^{-1}s^{-1} at high field, and the biggest one, 14 nm MNP-GA-PEG-OH with a hydrodynamic diameter in physiological medium of 32 nm and r_2 of 336 mM^{-1}s^{-1} at high field. A five times higher r_2 value in the 14 nm MNPs could lead to the use of less contrast agent material, therefore improving the efficiency and cost-effectiveness of the synthesis. Although at first sight the difference in size is not noticeable, at nanometer scale an increase of 60% in the hydrodynamic diameter could possibly affect the *in vivo* distribution and circulation times, which are two of the main concerns when considering the use of magnetic nanoparticles as contrast agents.[19, 31] Therefore, after intravenous injection of the MNPs, we followed the time-courses *in vivo* for 1 h in different tissues, and quantified T_2 changes at 0, 1, 24 and 48 h. For this purpose, 6 and 14 nm MNP-GA-PEG-OH (5 mg Fe-Mn per Kg of body weight) were intravenously injected in the tail vein of Balb/c mice, T_2-weighted MR images acquired every 2 minutes, and the time-courses calculated from regions of interest (ROIs) in kidneys, liver, spleen and muscle (Fig. 5). Both MNPs exhibited similar liver uptake rates (Fig. 5, black curves) with a maximum concentration of MNPs (maximal signal decay) at 6 min after injection, which remained stable for the rest of the time course. Significant kidney accumulation was also observed for both MNPs, as shown in Fig. 5 (red curves).
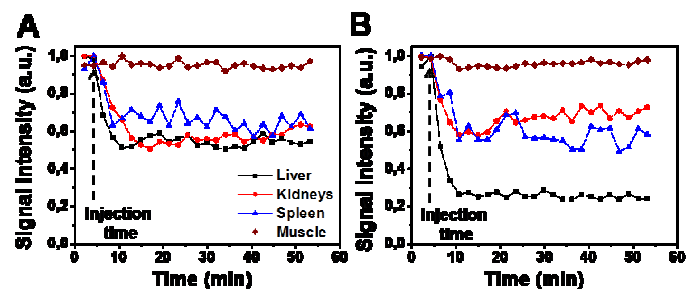

Fig. 5. *In vivo* time courses of MNP-GA-PEG-OH after intravenous injection in Balb/c mice. A) 6 nm MNP-GA-PEG-OH. B) 14 nm MNP-GA-PEG-OH.

Interestingly, some renal clearance seemed to happen as well (Fig. 6), in spite of the hydrodynamic diameters (HD) of our MNPs (20 and 32 nm), which exceed the well established size exclusion limit (6-8 nm) for glomerular filtration.[32] To demonstrate that our MNPs are partially excreted through the kidneys, we collected urine from 1 to 24 h after intravenous injection of our MNPs and analyzed it by transmission electron microscopy and Energy dispersive X-Ray (EDX) analysis (Fig. S8), which revealed the presence of the MNPs, although we could not verify their size due to interferences with the organic material present in the urine. A possible explanation for this phenomenon is that the MNPs shrink or lose part of the organic shell in the kidneys, likely related to the acidic environment, being thus able to cross the glomerular barrier. Muscles did not show any change in T_2 (Fig. 5, brown curve), indicating that, as expected, our MNPs did not reach the extravascular extracellular space.
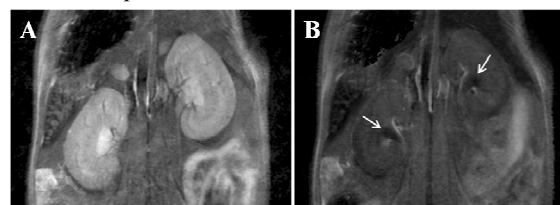

Fig. 6. Renal clearance of MNP-GA-PEG-OH. Kidneys before injection of the MNPs (A) and 12 minutes after injection (B), where accumulation of MNPs can be observed in the renal pelvis (white arrows).
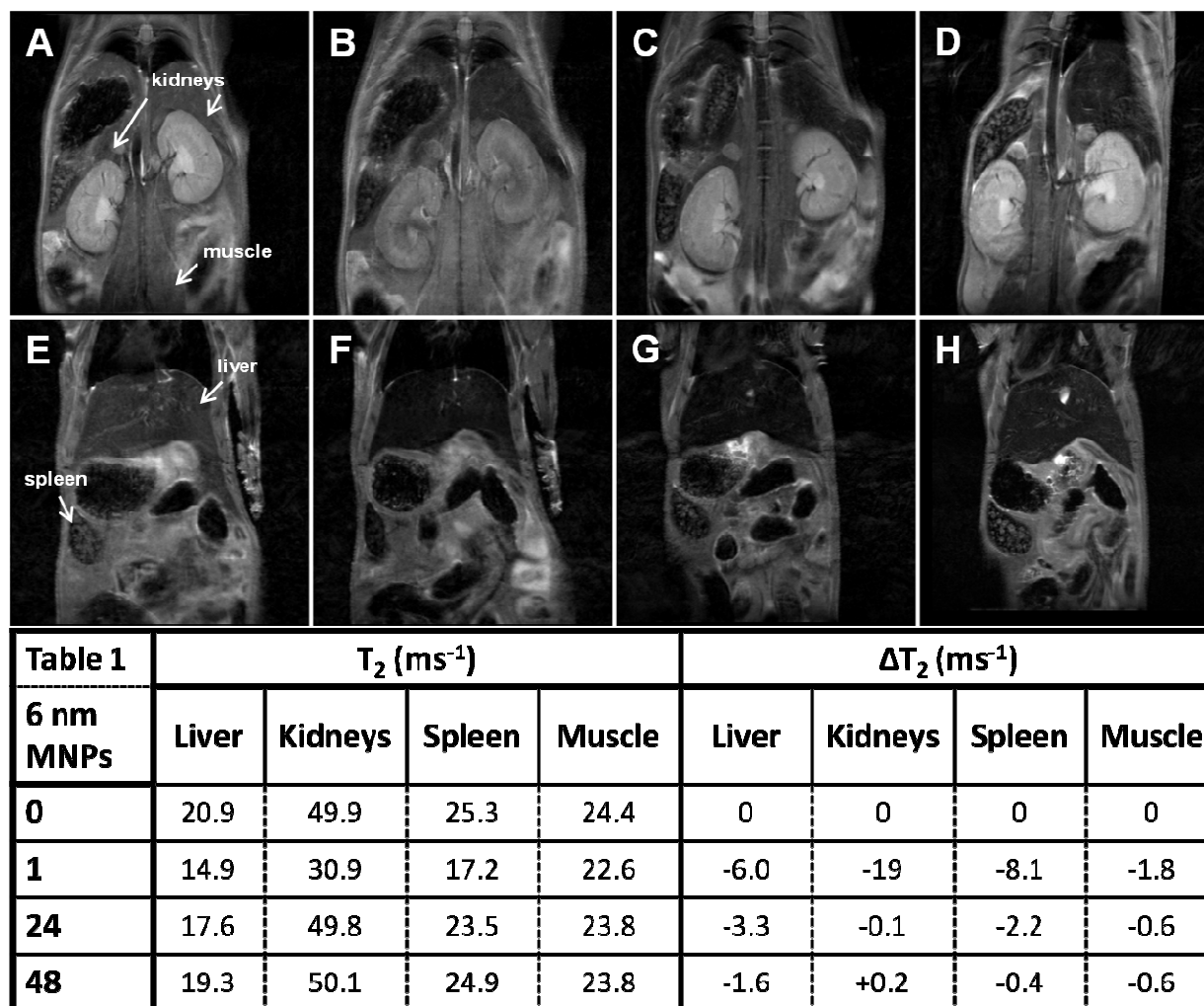
Table 1	T_2 (ms^{-1})				ΔT_2 (ms^{-1})			
6 nm MNPs	Liver	Kidneys	Spleen	Muscle	Liver	Kidneys	Spleen	Muscle
0	20.9	49.9	25.3	24.4	0	0	0	0
1	14.9	30.9	17.2	22.6	-6.0	-19	-8.1	-1.8
24	17.6	49.8	23.5	23.8	-3.3	-0.1	-2.2	-0.6
48	19.3	50.1	24.9	23.8	-1.6	+0.2	-0.4	-0.6

Fig. 7. Representative T_2-weighted MR images at different experimental times after the intravenous injection of 6 nm MNP-GA-PEG-OH. A-D) T_2-weighted images of kidneys and muscle at 0, 1, 24 and 48 h respectively after injection. E-H) T_2-weighted images of liver and spleen at 0, 1, 24 and 48 h after injection. Table 1 shows average T_2 and ΔT_2 values of the different tissues.

Long term clearance was evaluated by quantitative T_2 mapping at 0, 1, 24 and 48 h. Fig. 7 and Fig. 8 show representative high resolution T_2-weighted images and the T_2 values measured at the different experimental times. Both liver and kidneys showed significant decrease in T_2 at 1 h, with ΔT_2 of -6 and -7 in the liver and -19 and -19.8 in the kidneys for the 6 and 14 nm MNPs, respectively, indicating that our MNPs are slowly taken up by the reticuloendothelial system (RES), whereas they continue circulating in the bloodstream, and hence passing through the kidneys where they are partially excreted to urine, as mentioned above. As nicely shown by Choi *et al.*,[33] retention of PEGylated NPs within the renal corpuscles of the kidney cortex is size dependent, with maximal retention times for NPs in the range of 76-96 nm of hydrodynamic diameter, and virtually no retention at all for smaller NPs, with HD around 25 nm, which is very close to the HD of the MNPs reported herein. These small NPs were only found in peritubular capillaries. Hence, the MRI contrast detected in the kidneys can be attributed to circulating MNPs that pass through the peritubular

capillaries and return to the bloodstream until they are fully excreted through the liver. For the 6 nm MNPs the T_2 values recovered only partially in the liver after 48 h (ΔT_2 = -1.6), but were fully restored to normal values in the kidneys after 24 h (ΔT_2 = -0.1), suggesting that these MNPs are no longer circulating in the blood and that a small amount is still trapped in the kupffer cells after 48 h. However, for the 14 nm MNPs nor the liver neither the kidneys showed full recovery to normal T_2 values after 24 h, and only after 48 h the kidneys restored the normal values (ΔT_2 = +0.1), which suggests longer circulation times for these MNPs as compared to the smaller one. These circulation times are also in good agreement with those reported by Choi et al.,[33] where they described blood circulation half-lives ranging from 7 to 38 h for NPs with HD between 25 and 164 nm, being half-lives and HD inversely correlated. According to this findind, the 6 nm (20 nm HD) MNP is expected to have longer circulation times as compared to the 14 nm (32 nm HD) MNP. However, our data show the opposite. This finding could be explained by the unexpected

renal clearance we described above, which very likely acts more efficiently for the smaller one. The long circulating times together with the high relaxivity of our MNPs makes them an excellent candidate for MRI-based molecular imaging. In addition, the smaller MNPs, with sizes between 6 and 7.5 nm, show r_2/r_1 values within the intermediate range at 1.5 T, holding promise as dual contrast agents for clinical applications.
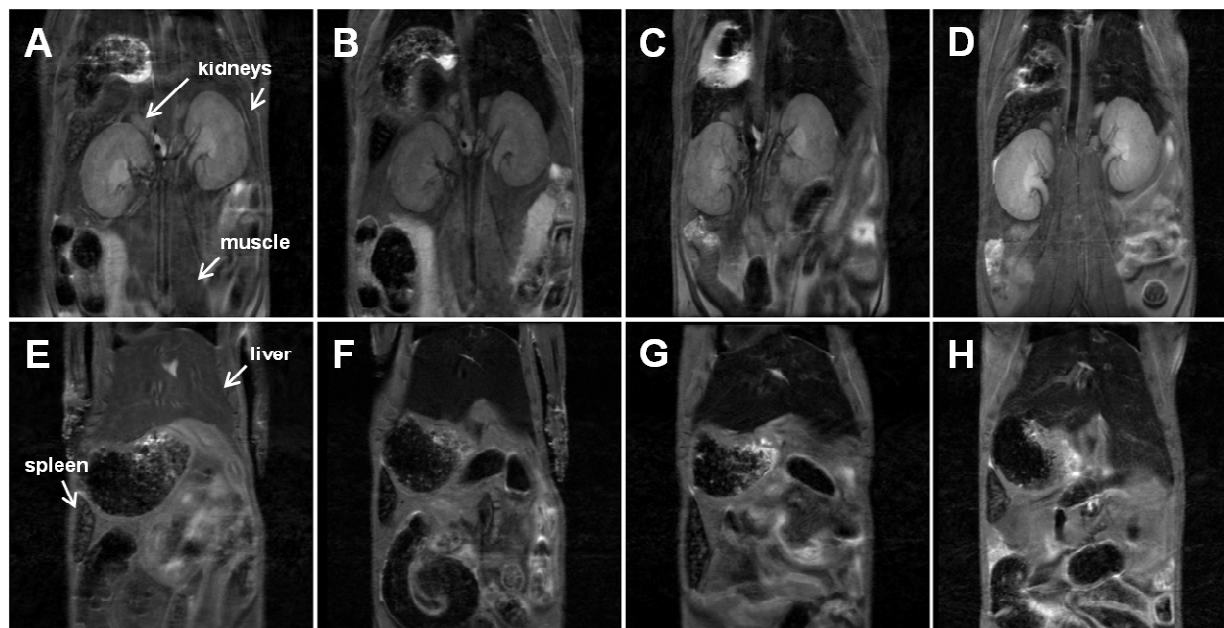

Table 2	T_2 (ms^{-1})				ΔT_2 (ms^{-1})			
14 nm MNPs	Liver	Kidneys	Spleen	Muscle	Liver	Kidneys	Spleen	Muscle
0	20.2	52.7	27	24.6	0	0	0	0
1	13.2	32.9	23.2	22.8	-7.0	-19.8	-3.8	-1.8
24	17.9	44.4	25.4	24.1	-2.3	-8.3	-1.6	-0.5
48	19.4	52.8	26.8	24.1	-0.8	+0.1	-0.2	-0.5

Fig. 8. Representative T_2-weighted MR images at different experimental times after the intravenous injection of 14 nm MNP-GA-PEG-OH. A-D) T_2-weighted images of kidneys and muscle at 0, 1, 24 and 48 h respectively after injection. E-H) T_2-weighted images of liver and spleen at 0, 1, 24 and 48 h after injection. Table 2 shows average T_2 and ΔT_2 values of the different tissues.

Experimental

Materials

Reagents were obtained from commercial suppliers and used without further purification. Iron (III) acetyl acetonate, Manganese (II) acetylacetonate, Oleic acid 99%, Oleylamine, Benzyl ether, 1,2-Hexanedecanediol, Gallic acid, Poly ethyleneglycol 3kDa, Triethylamine, 4-Dimethylaminopyridine were supplied by Sigma Aldrich and Acros Organics. As solvents, Milli-Q water (18.2 MΩ, filtered with filter pore size 0.22 μM) from Millipore, toluene, isopropanol, ethanol, acetone, hexane, and anhydrous tetrahydrofuran were used (HPLC grade, Acros Organics). Purification of the water-soluble magnetic nanoparticles from free reagents was performed on a centrifuge filters PALL with a molecular cut-off of 100 kDa. Dynamic light measurements were performed on a Zetasizer Nano ZS90 (Malvern, USA). FTIR spectra were recorded with a FTIR-4100 Jasco. ^{1}H-NMR spectrum was recorded on a NMR Bruker Ascend™ 400MHz spectrometer. Fe and Mn concentrations were determined on an Inductively Coupled Plasma High Resolution Mass Spectroscopy (ICP-HRMS, Element XR, Thermo Fisher). TEM images were obtained on a FEI Tecnai G2 Twin microscope operated at an accelerating voltage of 100 kV. TEM samples were prepared by dropping the solution on a carbon-coated copper grid and

letting the solvent evaporate. Thermogravimetric analysis (TGA) was carried out by using a METTLER TOLEDO model TGA/DSC 1 in the temperature range 30–800 °C with a heating rate of a 10 °C/min under N_2 flow (50 mL/min). X-ray diffraction patterns were collected with a PANalytical X´Pert PRO MPD diffractometer equipped with CuKα1 radiation in the 2θ range of 10-80°. Samples were prepared by dropcasting of a high concentrated magnetic nanoparticle solution onto a glass. The magnetization-field M-H curves were performed in a Vibrating Sample Magnetometer (VSM) at room temperature.

Synthesis of 3 kDa pegylated gallol anchor (Gallol-PEG)

The synthesis of ligand Gallol-PEG was performed similar to a previously established synthetic route, briefly 8.824 g of 3 kDa molecular weight polyethylene glycol (2.94 mmol), 0.5 g of gallic acid (2.94 mmol) and 71 mg of 4-Dimethylaminopyridine (DMAP, 0.294 mmol) were dissolved in 200 mL of anhydrous THF in a round bottom flask under inert atmosphere. A solution of Dicyclohexil carbodiimide (DCC) (3.03 g, 14.7 mmol, 50 mL THF) was drop wised to the mixture, and it was left stirred overnight at room temperature. The solid urea formed was filtered out and the solvent was removed in the rotaevaporator, yielding a crude gallol-PEG. The crude was dissolved in 200 mL of milli-Q water and adjusted to pH 2. In a separation funnel, the gallol-PEG was extracted from the aqueous phase with diclomethane (3 x 100 mL). The organic phase was concentrated under reduced pressure, yielding the corresponding gallol-PEG. 1H NMR (400 MHz, CDCl3) δ (ppm): 7.22 (s, Gallol-H), 4.43-4.40 (m, CH$_2$-ester), 3.85-3.45 (m, CH$_2$-PEG, -OH).

Synthesis of manganese ferrite nanoparticles (NPs)

Monodisperse manganese ferrite nanoparticles were synthesized following the seed-mediated growth protocol reported by Sun et al for iron oxide nanoparticles.

Synthesis of 6 $MnFe_2O_4$ nanoparticles seeds: 2 mmol of iron acetylacetonate, 1 mmol of manganese acetylacetonate, 10 mmol of hexadecanediol, 6 mmol of dodecylamine, 6 mmol of oleylamine and 20 mL of benzyl ether were mixed and magnetically stirred. The solution was heated to 200 °C for 2 h under a flow of nitrogen, followed by increasing the temperature to reflux (300 °C) for 1 h. The mixture was cooled down to room temperature by removing the heating mantle. Finally, the sample was washed several times using ethanol, acetone and isopropanol as precipitation agents and centrifugation, followed by re-dispersion in toluene.

Synthesis of 7.5 nm $MnFe_2O_4$ nanoparticles via 6 nm $MnFe_2O_4$ seeds: 80 mg of 6nm $MnFe_2O_4$ seeds dispersed in hexane (1 mL) were added to the mixture of 2 mmol of iron acetylacetonate, 1 mmol of manganese acetylacetonate, 10 mmol of hexadecanediol, 6 mmol of dodecylamine, 6 mmol of oleylamine and 20 mL of benzyl ether were mixed and magnetically stirred. The solution was heated to 60 °C for 1 h under vacuum to remove the hexane, and then the mixture was heated to 200°C for 2 h under a nitrogen flow. Soon after, the mixture was allowed to reflux (300 °C) for 1 h. The mixture

was cooled down to room temperature by removing the heating mantle. Finally, the sample was washed several times using ethanol, acetone and isopropanol as precipitation agents and centrifugation, followed by re-dispersion in toluene.

Similarly, 80 mg of 7.5 nm $MnFe_2O_4$ seeds reacted with 2 mmol of iron acetylacetonate, 1 mmol of manganese acetylacetonate, 10 mmol of hexadecanediol, 6 mmol of dodecylamine, 6 mmol of oleylamine and 20 mL of benzyl ether led to 9 nm $MnFe_2O_4$ nanoparticles. Using the same seed-growth procedure, 12 and 14 nm $MnFe_2O_4$ nanoparticles were synthesized.

Ligand exchange on manganese ferrite nanoparticles (MNPs)

Typically, a solution of 1.0 mL of Gallol-PEG (0.1 M in $CHCl_3$), 50 uL of triethylamine and 1.0 mL of oleic acid capped mangansese ferrite NPs (10 g/L in toluene) was shaking in a separation funnel. The mixture was diluted with 5 mL of toluene and 5 mL of Milli-Q water. After shaking, 10 mL of acetone was added to transfer completely the NPs into the aqueous phase. The aqueous phase was collected and placed in a rotaevaporator to remove the residual organic solvents. After that, the PEG-MNPs were purified in centrifuge filters PALL (Molecular weight cut-off: 100 kDa) at 450 rcf. The purification step was repeated minimum 3 times, adding physiological medium, till the filtered solution was completely clear. The solution of PEG-MNPs was placed onto a permanent magnet (0.6 T) for 5 min to remove the bigger aggregates.

***In vitro* Relaxivities**

T_1 and T_2 relaxivities were calculated at two different magnetic fields, 1.5 T (Bruker Minispec) and 9.4 T (Bruker Biospec) using concentrations of MNPs between 2.0 to 0.05 mM of Fe/Mn in physiological conditions, at 37 ºC.

T_1 was determined with an inversion-recovery sequence and T_2 with the Carl-Purcell-Meiboom-Gill (CPMG) sequence.

Cytotoxicity assays

The PC-3 human prostate cancer cell line was kindly provided by Dr. M. Japon (Department of Endocrine Tumorigenesis and Hormonal Regulation of Cancer, Biomedicine Institute of Seville, IBIS, CSIC-University of Seville, Spain). The cells were maintained in RPMI 1640 medium (BioWhittaker) supplemented with 10 % fetal bovine serum (BioWhittaker), 1% L-glutamin, 100 IU/mL penicillin and 100 IU/mL streptomycin (BioWhittaker) in a humidified atmosphere of 5 % CO_2 at 37 °C.   PC-3 cells were seeded overnight in 96-well plates at a density of 40.000 cells per well, in a final volume of 200 μL. For 3-[4,5-dimethylthiazol-2-yl]-2,5-diphenyl tetrazolium bromide (MTT) and lactate dehydrogenase (LDH) determinations, the media was replaced the day after with fresh media containing MNP-GA-PEG-OH at concentrations ranging from 100 μg/ml to 100 ng/ml for 24 h. After treatment, the supernatant of each well was saved for LDH measurement and replaced by 100 μL of media containing MTT labelling reagent (Roche Diagnostics GmbH, Mannheim, Germany) at a final concentration of 0.5 mg/mL. After further incubation for 4

hours in a humidified atmosphere (37 °C, 5% CO_2), 100 μ L of the solubilization solution was added to each well. The plates stood overnight in the incubator in a humidified atmosphere after complete solubilisation of the formazan crystals. Then, spectrophotometric absorbances were determined using a microplate (ELISA) reader at 570 nm with 660 nm as reference wavelength. LDH release after 24 h incubation with MNP-GA-PEG-OH was determined in the saved supernatant according to manufacturer's instructions (Roche Diagnostics GmbH, Mannheim, Germany). Each experimental condition was performed in triplicate. For detection of apoptotic cells by flow cytometry, PC-3 cells were seeded overnight in 12-well plates at a density of 120.000 cells per well, in a final volume of 1 mL, and treated as stated before. At the end of the experiment, the cells were fixed in an ice-cold solution of 70% ethanol for at least 24 h, incubated 10 minutes in DNA extraction buffer (Na_2HPO_4 0.2M, pH 7.8), and then incubated with 0.1% (w/v) RNAse and 50 μg/mL propidium iodide at 37ºC for 30 min before analysis for DNA content by flow cytometry using cell quest software.

In vivo MRI

Mice experiments were performed in accordance with the ethical guidelines of Andalusian government. Female Balb/c mice with ca. 30 g in weight, provided by Janvier Labs were used.

All the experiments were performed on a 9.4 T Bruker Biopec system equipped with a 400 mT/m gradients and a 40 mm quadrature bird-cage resonator. High resolution T_2-weighted images were acquired using a turbo-RARE sequence with respiratory gating (TE = 16 ms, TR = 1000 ms, 4 averages, 156 μm in-plane resolution and 1 mm slice thickness). Quantitative T_2 measurements were also performed using a multi-echo spin echo sequence (TEs ranging from 7 ms to 448 ms, TR = 3500 ms, FOV = 4 cm, matrix size = 128x128, slice thickness = 1 mm). The time-courses were followed by using a turbo-RARE with the same parameters indicated above, but only 1 average to improve temporal resolution (1 image every 2 minutes). The acquisition scheme was as follows: T_2-weighted, quantitative T_2, intravenous injection of the MNPs, time-course for one hour, quantitative T_2 and T_2 weighted. The MNPs were administered intravenously via tail vein at a concentration of 5 mg Fe/Mn per kg.

Conclusions

In this work, a new facile and fast ligand exchange method to transfer in aqueous media different sizes manganese iron oxide nanoparticles has been developed. A complete characterization over the nanoparticles confirmed the innocuous ligand exchange approach thus keeping the magnetic properties of the *as-prepared* MNPs, such as X-ray diffraction patterns of spinel metal ferrite crystal and high saturation magnetization values, and also these water soluble MNPs presented a low degree of cytotoxicity. The 6 nm MNP-GA-PEG-OH resulted to be good dual T_1 and T_2 contrast agents at clinical magnetic field, whereas the 14 nm MNP-GA-PEG-OH behave as excellent T_2 contrast agents at both low and high fields. The possibility to tune easily the low-cost ligand synthesis will enable to further functionalize the MNPs for targeting strategies. The water soluble MNPs displayed a high dense PEG core shell that prevents the rapid uptake by the reticuloendothelial system and permits long blood circulation times up to 24 h. The total clearance of the MNPs from the body took 24 h and 48 h for the 6 nm and 14 nm MNPs, respectively. The combination of low toxicity, excellent T_2 relaxation times, as well as excellent r_2/r_1 values at low field, together with long circulation times, make these nanomaterials a very promising contrast agent for MRI-based molecular imaging at clinical magnetic fields. The specific targeting of these MNPs could lead to the development of new methods for early diagnosis of different diseases and the tailoring healthcare to patients' individual needs through a personalized medicine approach based on MNPs.

Notes and references

[a]BIONAND, Andalusian Centre for Nanomedicine and Biotechnology, BIONAND (Junta de Andalucía-Universidad de Málaga), Parque Tecnológico de Andalucía, Málaga, Spain. E-mail: mpernia@bionand.es; mlgarcia@bionand.es.

[b]Institute of Nanoscience of Aragon, University of Zaragoza, Zaragoza, Spain

[c]CABIMER, Andalusian Center for Molecular Biology and Regenerative Medicine, Seville, Spain

[d]Department of Medical Biochemistry, Molecular Biology and Immunology, University of Seville, Seville, Spain

[e]Institute of Materials Science of Aragon, CSIC, University of Zaragoza, Spain

[f]Institute of Nano Biomedicine and Engineering, Shanghai Jiao Tong University, Shanghai, People's Republic of China.

† Electronic Supplementary Information (ESI) available: Additional experimental details included TEM images of MNPs, size distribution graphs, thermogravimetric analysis, FTIR spectra, and XRD patterns of MNPs. See DOI: 10.1039/b000000x/

1. R. A. Petros and J. M. Desimone, *Nature Reviews Drug Discovery*, 2010, 9, 615-627.
2. J. H. Lee, J. T. Jang, J. S. Choi, S. H. Moon, S. H. Noh, J. W. Kim, J. G. Kim, I. S. Kim, K. I. Park and J. Cheon, *Nature Nanotechnology*, 2011, 6, 418-422.
3. S. Mornet, S. Vasseur, F. Grasset and E. Duguet, *Journal of Materials Chemistry*, 2004, 14, 2161-2175.
4. J. H. Lee, Y. M. Huh, Y. W. Jun, J. W. Seo, J. T. Jang, H. T. Song, S. Kim, E. J. Cho, H. G. Yoon, J. S. Suh and J. Cheon, *Nature Medicine*, 2007, 13, 95-99.
5. M. Pernia Leal, A. Torti, A. Riedinger, R. La Fleur, D. Petti, R. Cingolani, R. Bertacco and T. Pellegrino, *ACS nano*, 2012, 6, 10535-10545.
6. F. Gazeau, M. Lévy and C. Wilhelm, *Nanomedicine*, 2008, 3, 831-844.
7. A. Figuerola, R. Di Corato, L. Manna and T. Pellegrino, *Pharmacological Research*, 2010, 62, 126-143.
8. P. Caravan, J. J. Ellison, T. J. McMurry and R. B. Lauffer, *Chem. Rev.*, 1999, 99, 2293-2352.
9. J. G. Penfield and R. F. Reilly Jr, *Nature Clinical Practice Nephrology*, 2007, 3, 654-668.
10. A. K. Gupta and M. Gupta, *Biomaterials*, 2005, 26, 3995-4021.
11. C. Tassa, S. Y. Shaw and R. Weissleder, *Accounts of Chemical Research*, 2011, 44, 842-852.
12. B. H. Kim, N. Lee, H. Kim, K. An, Y. I. Park, Y. Choi, K. Shin, Y. Lee, S. G. Kwon, H. B. Na, J. G. Park, T. Y. Ahn, Y. W. Kim, W. K. Moon, S. H. Choi and T. Hyeon, *Journal of the American Chemical Society*, 2011, 133, 12624-12631.
13. Z. Zhen and J. Xie, *Theranostics*, 2012, 2, 45-54.
14. Z. Li, S. X. Wang, Q. Sun, H. L. Zhao, H. Lei, M. B. Lan, Z. X. Cheng, X. L. Wang, S. X. Dou and G. Q. Max Lu, *Advanced Healthcare Materials*, 2013, 2, 958-964.
15. E. S. G. Choo, E. Peng, R. Rajendran, P. Chandrasekharan, C. T. Yang, J. Ding, K. H. Chuang and J. Xue, *Advanced Functional Materials*, 2013, 23, 496-505.
16. H. Yang, C. Zhang, X. Shi, H. Hu, X. Du, Y. Fang, Y. Ma, H. Wu and S. Yang, *Biomaterials*, 2010, 31, 3667-3673.
17. B. Sahoo, K. S. P. Devi, S. Dutta, T. K. Maiti, P. Pramanik and D. Dhara, *Journal of Colloid and Interface Science*, 2014, 431, 31-41.
18. J. Crossgrove and W. Zheng, *NMR in Biomedicine*, 2004, 17, 544-553.
19. M. Colombo, S. Carregal-Romero, M. F. Casula, L. Gutiérrez, M. P. Morales, I. B. Böhm, J. T. Heverhagen, D. Prosperi and W. J. Parak, *Chemical Society Reviews*, 2012, 41, 4306-4334.
20. T. Pellegrino, L. Manna, S. Kudera, T. Liedl, D. Koktysh, A. L. Rogach, S. Keller, J. Rädler, G. Natile and W. J. Parak, *Nano Letters*, 2004, 4, 703-707.
21. E. Amstad, T. Gillich, I. Bilecka, M. Textor and E. Reimhult, *Nano Letters*, 2009, 9, 4042-4048.
22. A. Riedinger, M. Pernia Leal, S. R. Deka, C. George, I. R. Franchini, A. Falqui, R. Cingolani and T. Pellegrino, *Nano Letters*, 2011, 11, 3136-3141.
23. S. Tong, S. Hou, Z. Zheng, J. Zhou and G. Bao, *Nano Letters*, 2010, 10, 4607-4613.
24. A. S. Karakoti, S. Das, S. Thevuthasan and S. Seal, *Angewandte Chemie - International Edition*, 2011, 50, 1980-1994.
25. E. Amstad, S. Zurcher, A. Mashaghi, J. Y. Wong, M. Textor and E. Reimhult, *Small*, 2009, 5, 1334-1342.
26. S. Sun, H. Zeng, D. B. Robinson, S. Raoux, P. M. Rice, S. X. Wang and G. Li, *Journal of the American Chemical Society*, 2004, 126, 273-279.
27. M. T. Peracchia, *S.T.P. Pharma Sciences*, 2003, 13, 155-161.
28. S. M. Moghimi, A. C. Hunter and J. C. Murray, *Pharmacological Reviews*, 2001, 53, 283-318.
29. M. P. Morales, S. Veintemillas-Verdaguer, M. I. Montero, C. J. Serna, A. Roig, L. I. Casas, B. Martínez and F. Sandiumenge, *Chemistry of Materials*, 1999, 11, 3058-3064.
30. P. Caravan, C. T. Farrar, L. Frullano and R. Uppal, *Contrast Media and Molecular Imaging*, 2009, 4, 89-100.
31. H. B. Na, I. C. Song and T. Hyeon, *Advanced Materials*, 2009, 21, 2133-2148.
32. M. Longmire, P. L. Choyke and H. Kobayashi, *Nanomedicine (Lond)*, 2008, 3, 703-717.
33. C. H. J. Choi, J. E. Zuckerman, P. Webster and M. E. Davis, *Proceedings of the National Academy of Sciences of the United States of America*, 2011, 108, 6656-6661.

Nanoscale Accepted Manuscript